

Geophysical and geochemical constraints on geoneutrino fluxes from Earth's mantle

Ondřej Šrámek^{a,*}, William F. McDonough^a, Edwin S. Kite^b, Vedran Lekić^a,
Stephen T. Dye^{c,d}, Shijie Zhong^e

^a*Department of Geology, University of Maryland, College Park, MD 20742, USA*

^b*Division of Geological and Planetary Sciences, California Institute of Technology,
Pasadena, CA 91125, USA*

^c*College of Natural Sciences, Hawaii Pacific University, Kaneohe, HI 96744 USA*

^d*Department of Physics and Astronomy, University of Hawaii, Honolulu, HI 96822 USA*

^e*Department of Physics, University of Colorado at Boulder, Boulder, CO 80309, USA*

Abstract

Knowledge of the amount and distribution of radiogenic heating in the mantle is crucial for understanding the dynamics of the Earth, including its thermal evolution, the style and planform of mantle convection, and the energetics of the core. Although the flux of heat from the surface of the planet is robustly estimated, the contributions of radiogenic heating and secular cooling remain poorly defined. Constraining the amount of heat-producing elements in the Earth will provide clues to understanding nebula condensation and planetary formation processes in early Solar System. Mantle radioactivity supplies power for mantle convection and plate tectonics, but estimates of mantle radiogenic heat production vary by a factor of up to 30. Recent experimental results demonstrate the potential for direct assessment of mantle radioactivity through observations of geoneutrinos, which are emitted by nat-

*Corresponding author

Email address: `sramek@umd.edu` (Ondřej Šrámek)

urally occurring radionuclides. Predictions of the geoneutrino signal from the mantle exist for several established estimates of mantle composition. Here we present novel analyses, illustrating surface variations of the mantle geoneutrino signal for models of the deep mantle structure, including those based on seismic tomography. These variations have measurable differences for some models, allowing new and meaningful constraints on the dynamics of the planet. An ocean based geoneutrino detector deployed at several strategic locations will be able to discriminate between competing compositional models of the bulk silicate Earth.

Keywords:

1. Introduction

The present-day Earth surface heat flux is 47 ± 1 (stat.) TW based on latest analysis of Davies and Davies (2010), in agreement with recent estimate of 46 ± 3 TW by Jaupart et al. (2007). The two contributors to the surface heat loss are secular cooling of the Earth, and heat generated by decay of long-lived radioactive isotopes of uranium, thorium, and potassium. The relative magnitude of these two components remain poorly constrained. Estimates of the present-day heat-producing element (HPE) abundances in the bulk silicate Earth (BSE, defined as the entire Earth less its metallic core) vary by a factor of about three between different models (O'Neill and Palme, 2008; Javoy et al., 2010; Arevalo et al., 2009; Turcotte and Schubert, 2002). Compositional estimates of depleted mantle (DM), which is the source of mid-ocean ridge basalt (MORB), vary by a similar factor (Workman and Hart, 2005; Salters and Stracke, 2004; Arevalo and McDonough, 2010). A distinct

15 chemical reservoir is usually invoked to account for the apparent deficit of
16 some elements and isotopes in the BSE chemical inventory (Hofmann, 1997).
17 Enriched in HPEs and some other elements (e.g., helium, argon), and possibly
18 “hidden” (i.e., untapped by surface volcanism; Boyet and Carlson, 2006),
19 this reservoir is usually assumed to be located in the lowermost mantle.
20 Because no methods exist for directly accessing and analyzing samples of
21 Earth’s deep mantle, compositional estimates rely on chemical analyses of
22 available rock samples (coming from a relatively shallow mantle at best),
23 interpretations of indirect evidence from geophysical data (e.g., seismology),
24 and a number of simplifying assumptions (e.g., relating Earth’s composition
25 to the Solar System or meteorite chemistry). Consequently, mass balances
26 for different chemical elements often yield inconsistent estimates of the size
27 and enrichment of the deep reservoir (Hofmann, 1997).

28 Recent advances in experimental neutrino physics provide a breakthrough
29 in deep-Earth research. Geoneutrino detections by KamLAND (Araki et al.,
30 2005; Gando et al., 2011) and Borexino (Bellini et al., 2010), using land-based
31 instruments, are consistent with flux predictions. These analyses assume a
32 planetary Th/U ratio and absence of U and Th in the core. Up to now, pre-
33 dictions of geoneutrino fluxes coming from the mantle consider spherically
34 symmetric HPE distributions, including uniform mantle and layers of vary-
35 ing depth and thickness (Araki et al., 2005; Bellini et al., 2010; Gando et al.,
36 2011; Mantovani et al., 2004; Enomoto et al., 2007; Fiorentini et al., 2007;
37 Dye, 2010). However, global seismic tomography reveals two large, low shear
38 velocity provinces (LLSVPs, also referred to as superplumes or thermochem-
39 ical piles) at the base of the mantle beneath Africa and the Pacific. Sharp

40 velocity gradients bound the LLSVPs (Wen et al., 2001), suggesting a compo-
 41 sitional difference from ambient lower mantle. This conclusion is supported
 42 by the observation that shear and sound wavespeeds are anti-correlated in
 43 the lowermost mantle (Su and Dziewonski, 1997). Moreover, existing mantle
 44 geoneutrino predictions are usually based on a single compositional model,
 45 even though several estimates for both BSE and DM composition exist.

46 Our new predictions of geoneutrino signal from the Earth’s mantle recog-
 47 nize the latest geophysical constraints and consider several established com-
 48 positional estimates for the Earth’s reservoirs. In section 2 we introduce the
 49 calculation of geoneutrino flux. Estimates of HPE abundances in BSE and
 50 the crust are discussed in section 3. Section 4 presents predictions of geoneu-
 51 trino emission from the mantle with various assumptions about HPE distri-
 52 bution, including a premise that seismically imaged deep-mantle structures
 53 may reflect a compositional difference. Section 5 focuses on detectability
 54 of predicted mantle flux lateral variations, followed by general discussion in
 55 section 6.

56 2. Geoneutrino flux calculation

57 Beta-decays in decay chains of radionuclides ^{238}U , ^{235}U , ^{232}Th and β -
 58 decay of ^{40}K produce electron antineutrinos. The antineutrino flux $\Phi_X(\mathbf{r})$
 59 at position \mathbf{r} from a radionuclide X at positions \mathbf{r}' distributed in a spatial
 60 domain Ω is calculated from

$$\Phi_X(\mathbf{r}) = \frac{n_X \lambda_X \langle P \rangle}{4\pi} \int_{\Omega} \frac{a_X(\mathbf{r}') \rho(\mathbf{r}')}{|\mathbf{r} - \mathbf{r}'|^2} d\mathbf{r}', \quad (1)$$

61 where n_X is the number of antineutrinos per decay chain, λ_X is the decay
62 constant (1/lifetime), a_X is the abundance of radioactive isotope (number of
63 atoms of radioactive isotope per unit mass of rock), and ρ is rock density
64 (Mantovani et al., 2004). The average survival probability $\langle P \rangle = 0.58$ as-
65 sumes a signal source region size much larger than the neutrino oscillation
66 length (60–110 km depending on antineutrino energy; see, e.g., Dye, 2012, for
67 more extensive discussion). The isotopic abundance a_X is calculated from

$$a_X = \frac{A_X X_X}{M_X}, \quad (2)$$

68 where A_X is the elemental abundance (mass of element per unit mass of
69 rock), X_X is the isotopic ratio (atoms of radionuclide per atoms of element),
70 M_X is atomic mass. Radiogenic heating rate H_X (power per unit mass of
71 rock) by radionuclide X is calculated from

$$H_X = a_X \lambda_X Q_X^h, \quad (3)$$

72 where Q_X^h is the energy (per decay) available for radiogenic heating. Values
73 of atomic parameters in equations (1–3) are listed in Table 1. Input from
74 geochemistry and geophysics is required for the elemental abundances A_X
75 and rock density ρ . For a spherical shell source region with uniform rock
76 density and uniform radionuclide abundance, the flux (1) can be evaluated
77 analytically (Krauss et al., 1984; Fiorentini et al., 2007).

78 Current experimental methods for geoneutrino detection, which employ
79 the neutron inverse β -decay reaction, are only able to detect the highest
80 energy geoneutrinos from ^{238}U and ^{232}Th decay chains. The conversion fac-
81 tor between the signal (geoneutrino flux) and a measurement (number of

82 detected events) is a function of the detector size (number of free target pro-
 83 tons), experiment duration (live-time) and detection efficiency. A convenient
 84 “terrestrial neutrino unit” (TNU) was devised as 1 event detected over 1
 85 year exposure of 10^{32} target protons at 100% detection efficiency (Manto-
 86 vani et al., 2004). One TNU corresponds to a flux of $7.67 \times 10^4 \text{ cm}^{-2} \text{ s}^{-1}$
 87 from ^{238}U or $2.48 \times 10^5 \text{ cm}^{-2} \text{ s}^{-1}$ from ^{232}Th (Enomoto et al., 2007). The
 88 conversion for a combined signal from ^{238}U and ^{232}Th depends on the Th/U
 89 abundance ratio of the source; for $\text{Th}/\text{U} \approx 4$ about 80% of the measured
 90 events comes from ^{238}U and the remaining 20% from ^{232}Th (see, e.g., Dye,
 91 2012, for detailed description).

92 **3. HPE abundances in BSE and the crust**

93 Three classes BSE compositional estimates – termed here “cosmochem-
 94 ical”, “geochemical”, and “geodynamical” – give different abundances of
 95 HPEs. The cosmochemical approach bases Earth’s composition on enstatite
 96 chondrites, which show the closest isotopic similarity with mantle rocks and
 97 have sufficiently high iron content to explain the metallic core (Javoy et al.,
 98 2010). Cosmochemical estimates suggest relatively low HPE abundances.
 99 Following Javoy (personal communication), we assume bulk Earth uranium,
 100 thorium and potassium abundances of $A_U = 8.0 (\pm 20\%) \text{ ppb}$, $A_{Th} = 28.8 (\pm 10\%) \text{ ppb}$,
 101 $A_K = 87.5 (\pm 20\%) \text{ ppm}$. We then multiply these values by the enrichment
 102 factor for refractory lithophile elements of 1.479 that accounts for the differ-
 103 entiation of an early Earth into core and mantle (Javoy et al., 2010), and get
 104 U, Th, and K abundances in BSE of $12 \pm 2 \text{ ppb}$, $43 \pm 4 \text{ ppb}$, and $129 \pm 26 \text{ ppm}$,
 105 respectively.

106 There are other low Earth models that have similarly low abundance of
107 the heat producing elements. O'Neill and Palme (2008) recently proposed a
108 model whereby the early Earth was developing a crust, enriched in highly in-
109 compatible elements (e.g., U, Th, and K) that experienced collisional erosion,
110 which resulted in marked depletions of these elements from the bulk silicate
111 Earth. Consequently, the O'Neill and Palme model has a bulk silicate Earth
112 that contains as little as 10 ppb U, 40 ppb Th and 140 ppm K, which is, in
113 terms of absolute concentration, comparable to the Javoy et al. model.

114 Geochemical estimates adopt chondritic compositions for the relative
115 abundances of refractory lithophile elements with absolute abundances con-
116 strained by terrestrial samples (McDonough and Sun, 1995), and have mod-
117 erate abundances of HPEs. We use a geochemical estimate of Arevalo et al.
118 (2009), which is a modified version of McDonough and Sun's (1995) model.
119 The uncertainties are included, and within the errors the proposed values are
120 consistent with other geochemical estimates (Hart and Zindler, 1986; Allègre
121 et al., 1995; Palme and O'Neill, 2003).

122 Geodynamical estimates are based on the energetics of mantle convection
123 and the observed surface heat loss (Turcotte and Schubert, 2002). Clas-
124 sical parameterized thermal evolution models require a significant fraction
125 ($\gtrsim 60\%$) of the present-day mantle heat output to be contributed by ra-
126 diogenic heating in order to prevent extremely high temperatures in Earth's
127 early history, which is ruled out by geological observations. This is commonly
128 expressed in terms of the mantle Urey ratio, defined as mantle radiogenic heat
129 production over total heat output from the mantle. The mantle Urey ratio
130 characterizes the energy available for mantle convection and plate tectonics,

131 which is mostly accretional energy from Earth formation for $Ur < 0.5$, and
132 mostly ongoing radioactivity for $Ur > 0.5$. Our geodynamical HPE abun-
133 dance estimate is based on values of Turcotte and Schubert (2002), scaled
134 to result in mantle Urey ratio of 0.6–0.8. Table 2 lists the U, Th, and K
135 abundances and the Th/U and K/U mass ratios for the three BSE compo-
136 sition estimates. The rates of radiogenic heat production are 11 ± 2 TW,
137 20 ± 4 TW and 33 ± 3 TW for the cosmochemical, geochemical and geody-
138 namical estimates, respectively. Including the uncertainties, the predicted
139 radiogenic heat production in BSE varies by a factor of four.

140 The bulk composition of the crust is relatively well defined. Our crustal
141 model is constructed using CRUST2.0 (Bassin et al., 2000) crustal structure
142 including the densities of the layers. We treat the ‘A’ and ‘B’ type tiles of the
143 CRUST2.0 model as oceanic and all other tiles as continental. We use HPE
144 abundance estimates of Rudnick and Gao (2003) “R&G” for the continental
145 crust and sediments. Abundances of the HPE in the oceanic crust are taken
146 from White and Klein (2013, projected) “W&K”, and for oceanic sediments
147 we use those of Plank and Langmuir (1998) “P&L”. Consequently, the con-
148 tinental crust (CC) generates 7.8 ± 0.9 TW of radiogenic power, whereas the
149 oceanic crust (OC) only gives off 0.21 ± 0.03 TW (Table 2).

150 4. Geoneutrino emission from Earth’s mantle

151 4.1. Isochemical mantle models

152 From the radiogenic heat production in the BSE and the crust we calcu-
153 late bulk mantle (BM) composition by a simple mass balance,

$$A_X^{BSE} m^{BSE} = A_X^{BM} m^{BM} + A_X^{CC} m^{CC} + A_X^{OC} m^{OC}, \quad (4)$$

154 where A_X^Y is the elemental abundance of element X in reservoir Y , and m^Y
 155 is the mass of the reservoir (Table 3). Equation (4) assumes negligible ra-
 156 dioactivity in the core (McDonough, 2003). The input elemental abundances
 157 for BSE, CC, and OC, the reservoir masses, and BM abundances are listed
 158 in Table 2. The resulting mantle Urey ratios amount to 0.07 ± 0.05 , 0.3 ± 0.1
 159 and 0.7 ± 0.1 for the cosmochemical, geochemical, and geodynamical BSE
 160 estimates. The mantle radiogenic heat production can be as low as 0.9 TW
 161 (low-end cosmochemical BSE) and as high as 28 TW (high-end geodynamical
 162 BSE), that is, a variation by a factor of ~ 30 .

163 We use the bulk mantle HPE abundances to predict geoneutrino fluxes at
 164 Earth’s surface from a spherical-shell mantle of uniform composition (model
 165 UNIF in Figure 1a). We account for the density increase with depth by a
 166 factor of roughly two across the mantle using PREM (Dziewonski and An-
 167 derson, 1981), which also gives the radii of the surface (6371 km), the top of
 168 the mantle (6346.6 km) and the CMB (3480 km). Here we neglect the varia-
 169 tion in the crust–mantle boundary depth; however, the MOHO topography
 170 is accounted for later when we combine the fluxes from the mantle with the
 171 crustal flux. The calculated mantle geoneutrino fluxes from $^{238}\text{U} + ^{232}\text{Th}$, in
 172 $\text{cm}^{-2} \mu\text{s}^{-1}$, are 0.28 ± 0.19 , 1.1 ± 0.3 , and 2.5 ± 0.3 for the three BSE estimates
 173 (Table 4, black symbols in Figure 1b).

174 4.2. Layered mantle models

175 A chemically uniform mantle with either geochemical or geodynamical
 176 HPE abundances is at odds with analyses of MORB sample compositions,
 177 which commonly require a MORB source rock depleted in HPEs relative to
 178 a bulk mantle. We consider several available compositional estimates for

179 the depleted MORB-source mantle, as given by Workman and Hart (2005)
 180 “W&H”, Salters and Stracke (2004) “S&S”, and Arevalo and McDonough
 181 (2010) “A&McD”, listed here from the “coldest” (most depleted in HPEs) to
 182 the “warmest” compositions (Table 2). The DM model of A&McD is based
 183 on a global MORB composition and it deviates from the modeling used in
 184 Arevalo et al. (2009), where they estimated the composition of the DM using
 185 differing proportions of N-MORB and E-MORB.

186 We consider two mantle reservoirs: a depleted mantle with DM compo-
 187 sition above and enriched mantle (EM) below, where the reservoir masses
 188 satisfy $m^{BM} = m^{DM} + m^{EM}$. The elemental mass balance is then

$$A_X^{BM} m^{BM} = A_X^{DM} m^{DM} + A_X^{EM} m^{EM}. \quad (5)$$

189 We define the mass fraction of the enriched reservoir, $F^{EM} = m^{EM}/m^{BM}$,
 190 and the enrichment factor, $E_X = A_X^{EM}/A_X^{DM}$, and rewrite equation (5) as

$$A_X^{BM} = A_X^{DM} [1 + (E_X - 1)F^{EM}]. \quad (6)$$

191 For given BM and DM compositional estimates, a trade-off exists between
 192 the enrichment and the mass fraction of the enriched mantle (EM) reservoir –
 193 for a prescribed DM composition, a smaller enriched reservoir mass requires
 194 larger chemical enrichment to satisfy a specified bulk mantle composition.

195 The size of the enriched geochemical reservoir is not well constrained,
 196 with model values spanning a few percent to a few tens of percent of mantle
 197 by mass. We consider an enriched reservoir containing 10% of mantle mass.
 198 Enrichment factors E for various combinations of BSE and DM estimates,
 199 calculated from the “BSE=Crust+DM+EM” mass balance of equations (4–
 200 6), are listed in Table 4. For cosmochemical BSE based on enstatite chondrite

201 chemistry, this exercise results in either minimal enrichments or even defi-
 202 ciencies in HPEs, making the cosmochemical estimate consistent with the
 203 absence of an enriched reservoir. Cosmochemical bulk mantle is too depleted
 204 to be consistent with A&McD depleted mantle estimate at 1σ uncertainty
 205 level. It is also deficient in potassium when combined with S&S or W&H DM
 206 abundances, and both uranium and thorium relative to S&S, however consis-
 207 tent with these DM estimates when the uncertainty is considered (Table 4).
 208 In cases where formal evaluation and error propagation lead to enrichment
 209 factors smaller than one (the “enriched reservoir” would actually be depleted
 210 relative to “depleted mantle”) or negative (i.e., a deficiency in a particular
 211 element), we limit the minimum permissible enrichment value to one (i.e.,
 212 uniform mantle composition).

213 We calculate geoneutrino fluxes from a spherically symmetric two-reservoir
 214 mantle where the reservoir potentially enriched in HPEs is a 427 km thick
 215 layer immediately above CMB (model EL in Fig. 1a). The predicted fluxes,
 216 including uncertainties, are plotted in Figure 1b as red, green and blue sym-
 217 bols (also listed in Table 4). Relative to a uniform HPE distribution, a
 218 decrease in flux of geoneutrinos results when HPEs are sequestered at the
 219 bottom of the mantle, i.e., further from the measurement location at the
 220 Earth’s surface (Dye, 2010).

221 What is the maximum possible flux reduction by such sequestration for
 222 a given bulk mantle HPE abundances? Maximum flux Φ_{max} is obtained for
 223 uniformly distributed HPEs (no enrichment, $E = 1$); we exclude the dynam-
 224 ically implausible arrangement, where the deep mantle would be depleted in
 225 HPEs relative to the overlying mantle. Minimum possible flux Φ_{min} would be

226 obtained in the hypothetical case where all HPEs were sequestered near CMB
 227 and the remaining mantle were HPE-free (maximum enrichment, $E \rightarrow \infty$).
 228 In between these limit values, with increasing enrichment factor E the flux
 229 Φ decreases proportionally to the depletion of the upper mantle. Using eqn.
 230 (6) we get

$$\Phi(E) = \Phi_{min} + \frac{\Phi_{max} - \Phi_{min}}{1 + (E - 1)F^{EM}}. \quad (7)$$

231 It is instructive to plot the normalized flux $\Phi(E)/\Phi_{max}$, which shows the flux
 232 reduction relative to a mantle with uniform HPE distribution (Figure 1c).
 233 The normalized minimum flux Φ_{min}/Φ_{max} for the EL model (enriched layer of
 234 uniform thickness) can be obtained analytically for a uniform density mantle.
 235 PREM density mantle requires a simple integration and Φ_{min}/Φ_{max} is 0.76 for
 236 F^{EM} of 10 %. The inset in Figure 1c shows the relatively weak dependence
 237 of this flux reduction limit on the mass fraction of the enriched layer.

238 4.3. Models using a seismically constrained mantle structure

239 To illustrate the effect of possible lateral variation in the enriched reservoir
 240 geometry (e.g., LLSVPs or piles), we first consider axially symmetric cases
 241 with either a single deep-mantle pile or two antipodal piles (models P1 and
 242 P2, Figure 1a). Model P1 is an idealized single 1000-km thick “pile” with
 243 vertical sides and lateral extent 0–76°, sitting on the CMB. Model P2 has two
 244 antipodal piles of thickness 1000 km and lateral extent 0–52°. The piles in
 245 both models contain 10% of the mantle by mass. The predicted geoneutrino
 246 fluxes from the mantle vary along latitude (Figure 1d and Table 4). We used
 247 geochemical BSE and A&McD DM abundances, which lead to enrichment
 248 in U and Th within the piles by a factor of 6.0 and 12, respectively. Both

models generate a surface-averaged flux which is basically identical (larger by 1%) to the flux in the spherically symmetric EL model with the same HPE abundances. Model P1 shows a flux variation of $^{+31\%}_{-22\%}$ amplitude about the average value, and model P2 shows a somewhat smaller variation of $^{+19\%}_{-10\%}$ amplitude about the surface average. The significant spatial variation of geoneutrino fluxes from the mantle motivates more detailed models of mantle geoneutrino emission.

We examine an enriched reservoir geometry that is based on seismic images of the deep mantle. We use seismic tomography model S20RTS (Ritsema et al., 1999) and consider a simple mapping from shear-wave speed V_S to enriched reservoir shape: slow regions with V_S anomaly below -0.25% relative to PREM (Dziewonski and Anderson, 1981) and which are deeper than 1500 km are assigned as enriched material. The remaining volume is assumed to be depleted mantle (model TOMO; Figure 1a). This parameterization gives an enriched reservoir containing 9.5 % of the mantle by mass (or 8.2 % by volume), while 90.5 % is depleted mantle, i.e., proportions very similar to the previously presented two-reservoir mantle models, thus resulting in similar enrichment.

The calculated mantle geoneutrino fluxes from the U and Th decay chains vary with geographical location; a global map for one particular case using geochemical BSE and A&McD DM abundances is shown in Figure 2. The surface-averaged flux is very close to the spherically symmetric EL model value (2% larger; Table 4). The amplitude of the flux variation is $^{+25\%}_{-13\%}$ relative to the spatial mean of $1.0 \text{ cm}^{-2} \mu\text{s}^{-1}$ ($^{238}\text{U} + ^{232}\text{Th}$) for the enrichment factors 6.3 and 13 for U and Th, respectively. Two flux maxima – one

274 at 125% of average signal in southwestern Africa (9° S 13° E), the other at
 275 121% in Central Pacific (9° S 161° W) – are related to the African and Pa-
 276 cific deep mantle piles. The surrounding low flux region is broader and less
 277 pronounced. The absolute minimum at 87% of the average is at 48° N 104° E
 278 (Mongolia). Mantle geoneutrino flux maps for all possible combinations of
 279 BSE and DM compositional estimates, including propagation of the uncer-
 280 tainties show that though the spatial pattern of the flux remains identical
 281 for all cases – we use the same tomography-to-enriched reservoir mapping,
 282 the surface-averaged flux and the amplitude of variation is dependent on
 283 the compositional model (Supplementary Figures S1, S2; Table 4 reports
 284 the average, minimum, and maximum flux based on the central values of
 285 the compositional estimates). If the piles are compositionally distinct as in-
 286 dicated by geophysics, and correspond to the hidden reservoirs as inferred
 287 from geochemistry, then the geoneutrino flux exhibits a dipolar pattern.

288 *4.3.1. Effect of mantle piles' size on geoneutrino flux*

289 The size of the possible enriched reservoir is not well constrained from
 290 geochemical analyses. Seismic modeling defines the chemical piles beneath
 291 Africa at $\sim 5 \times 10^9$ km³ (or $\sim 0.6\%$ volume) (Wang and Wen, 2004) and a
 292 similar size beneath the Pacific. This is smaller than the enriched volume
 293 fraction of 8% we obtained by using a cut-off contour of $\delta V_s = -0.25\%$ of
 294 seismic model S20RTS (Ritsema et al., 1999) to trace the enriched man-
 295 tle reservoir boundary. We investigate how the mantle geoneutrino flux at
 296 Earth's surface changes when different δV_s cut-off contour is used. More
 297 negative δV_s cut-off results in a smaller enriched reservoir size, while the
 298 enrichment factor E (relative to depleted mantle composition) is larger in

order to yield a given bulk mantle composition (Table 5). Maps of mantle geoneutrino flux at the surface calculated for several different choices of δV_s cut-off contour are shown in Figure 3. They show similar spatial pattern and comparable amplitudes.

5. Is lateral variation in mantle geoneutrino flux resolvable?

Measurements of geologically interesting antineutrinos include the detections of mantle (M) and crust (C) geoneutrinos, reactor (r) antineutrinos, and other antineutrino background (bg). The total event rate R (in TNU) is

$$R = R_M + R_C + R_r + R_{bg}. \quad (8)$$

After detector exposure ε (in TNU^{-1} or $10^{32} \text{ proton yr}$) the expected total antineutrino count N is

$$N = \varepsilon R. \quad (9)$$

The exposure ε is calculated from the detector of size P (in units of 10^{32} free protons), detection efficiency e ($0 < e \leq 1$) and live-time T (in yr),

$$\varepsilon = ePT. \quad (10)$$

A 10-kiloton detector contains about 8×10^{32} free protons, therefore a year-long operation gives an exposure of $\sim 8 \text{ TNU}^{-1}$ (assuming 100% detection efficiency).

The detection count has a statistical error

$$\delta N_{\text{stat}} = \sqrt{N}. \quad (11)$$

Systematic errors come from instrumental error (in particular uncertainty $\delta\varepsilon$ in detector exposure), and the uncertainties in geological, reactor, and

background signals. The uncertainty in mantle geoneutrino detection δR_M ,
written in terms of event rates and their errors, is obtained from (Dye, 2010)

$$(\delta R_M)^2 = \frac{R}{\varepsilon} + \left(\frac{R}{\varepsilon}\right)^2 (\delta\varepsilon)^2 + (\delta R_C)^2 + (\delta R_r)^2 + (\delta R_{bg})^2, \quad (12)$$

where the first term on the right is the statistical error, followed by contributions to the systematic error: exposure, crust, reactor, background.

Mantle geoneutrino determination at existing and proposed continental detection sites is limited by the uncertainty in crustal radioactivity. The dominance of crustal signature is clearly visible in Figure 4, which maps total geoneutrino signal from crust + mantle (Figure 4a), and the fraction of the signal that is contributed by the mantle (Figure 4b). In this calculation, MOHO topography is accounted for and the geoneutrino fluxes are evaluated at zero elevation in oceanic areas and at the Earth’s surface (positive elevation) in continental regions.

Inspection of Figure 4b suggests that the Pacific ocean basin offers the highest mantle-to-crust geoneutrino flux ratio. In Figure 4c we show the variation of the predicted geoneutrino signal along the meridian at 161°W which intersects the Pacific mantle flux maximum at 9°S. The crustal flux remains low between 40°N and 65°S at 3.5–4 TNU ($\pm 15\%$ uncertainty), while emission from the mantle varies between 2.5 and 36 TNU depending on mantle compositional model and measurement location. Mantle composition based on geodynamical BSE estimate results in highest geoneutrino fluxes and strongest spatial variation, a cosmochemical mantle model generates a small spatially uniform flux, and mantle based on geochemical BSE abundances is intermediate between the two. Importantly, even with uncertainty considered, the three BSE estimates result in distinct mantle geoneutrino predictions at 1σ

341 level (Figures 4c and 5).

342 In line with the general suggestion of Dye (2010), we propose that geoneu-
343 trino detection at two sites in the Pacific ocean is the best shot at constraining
344 mantle U and Th abundances, and examining the thermochemical piles (su-
345 perplumes) hypothesis. Site #1 should be the location of the predicted Pa-
346 cific mantle flux maximum (161°W 9°S, Figure 4). Site #2 should be remote
347 from site #1 so that the predicted mantle flux variation can be pronounced,
348 while also sufficiently distant from continental crust in order to keep a fa-
349 vorable mantle-to-crust flux ratio; a good candidate is Southern Pacific (e.g.,
350 161°W 60°S, some 50 degrees directly south of site #1, Figure 4). The inputs
351 for calculation of detection uncertainty δR_M (eqn. 12) at each measurement
352 site are $R_C \pm \delta R_C$, $R_r \pm \delta R_r$, $R_{bg} \pm \delta R_{bg}$, and R_M (Table 6). A reasonable esti-
353 mate for reactor background (r) uncertainty is $\pm 5\%$ – the uncertainties in the
354 spectrum and cross section contribute $\sim 2\%$, and further uncertainty is asso-
355 ciated with power records from reactors, the oscillation parameters, and the
356 reactor antineutrino anomaly (Dye, 2012). Other background (bg) consists
357 of four primary sources: $^{13}\text{C}(\alpha, n)^{16}\text{O}$ reaction, fast neutrons from cosmic
358 muons outside detector, long-lived neutron unstable radionuclides (^9Li , ^8He)
359 cosmogenically produced inside the detector, and accidentals. Borexino team
360 estimated the background signal at 2.3 ± 0.3 TNU (Bellini et al., 2010) and
361 we use this value as a conservative estimate; see more detailed discussion by
362 Dye (2012).

363 Figure 5a shows the predicted geoneutrino signal at proposed site #1 at
364 the Pacific flux maximum against prediction at site #2 in Southern Pacific.
365 The detector exposure, necessary to discriminate between the predicted lat-

366 eral variation in flux and a spherically uniform mantle emission, depends on
 367 the unknown mantle HPE abundances. The region of detectable difference
 368 between predictions from a “piles” model and from a uniform mantle model
 369 is highlighted in Figure 5a. Exposure $\lesssim 10 \text{ TNU}^{-1}$ is sufficient to resolve the
 370 variation predicted from geodynamical BSE models at 1σ uncertainty level.
 371 The lateral variation is resolvable for the high-abundance end of the geochem-
 372 ical BSE model with exposures from ~ 10 to few tens TNU^{-1} (Figure 5b).
 373 Cosmochemical predictions and the low end of geochemical predictions pro-
 374 duce a mantle essentially uniform in composition.

375 **6. Discussion**

376 Combined analysis of KamLAND (Araki et al., 2005; Gando et al., 2011)
 377 and Borexino (Bellini et al., 2010) antineutrino observations places the bounds
 378 on mantle geoneutrino event rate at $23 \pm 10 \text{ TNU}$ where the Th/U ratio
 379 spans a range of 2.7–3.9 (Fiorentini et al., 2012). This translates into a
 380 mantle geoneutrino flux of $1.2\text{--}3.7 \text{ cm}^{-2} \mu\text{s}^{-1}$, i.e., a result with a relatively
 381 large error, which supports both geodynamical and geochemical BSE models,
 382 but is incompatible with cosmochemical BSE (and collisional erosion mod-
 383 els such as O’Neill and Palme, 2008) at 1σ level (Figure 1b). KamLAND
 384 now benefits from significant decrease of nuclear reactor signal after power
 385 plant shutdowns following the Fukushima Daiichi accident. Borexino’s re-
 386 sult is dominated by statistical uncertainty, which decreases with continuing
 387 measurement. New experiments capable of geoneutrino detection are being
 388 developed. In 2013 the SNO+ detector at SNOLab in Ontario, Canada, is
 389 expected to go on-line. The LENA experiment is proposed either at the

390 Pyhäsalmi mine (near Pyhäjärvi, Finland), or at the Laboratoire Souterrain
391 de Modane (near Fréjus, France; Wurm et al., 2012). Reduction of instrumen-
392 tal uncertainty and more precise description of crustal geology, particularly
393 in the vicinity of neutrino experiment sites, are expected increase sensitivity
394 to the distribution of Earth’s internal radioactivity.

395 The debate about the chemical composition of the silicate Earth remains
396 open. Latest studies find support for both enstatite chondrite-based “cosmo-
397 chemical” composition (Warren, 2011; Zhang et al., 2012) and carbonaceous
398 chondrite-based “geochemical” composition (Murakami et al., 2012), some
399 propose a more complicated chondrite mix (Fitoussi and Bourdon, 2012), or
400 argue against a chondritic Earth altogether (Campbell and O’Neill, 2012).
401 Geoneutrinos can supply the key missing evidence necessary to refine our
402 knowledge of Earth’s heat engine. If BSE abundances turn out to be close to
403 the low cosmochemical estimate, for example, geophysics will be challenged
404 to explain the present-day high surface heat flux. Detection of lateral vari-
405 ation in the mantle geoneutrino flux – or absence thereof – will stimulate
406 further well-posed questions about the stability and dynamics of the chem-
407 ical piles, and the origin and nature of the seismically imaged deep-mantle
408 structures. These questions clearly motivate experimental efforts to constrain
409 mantle radioactivity by geoneutrino detection.

410 Our finding support the potential for doing neutrino tomography of the
411 mantle. From the perspective of deep-Earth research, the desired location
412 for a geoneutrino detector is an oceanic site far away from continental crust;
413 an oceanic transportable detector is proposed for the Hanohano experiment
414 (Learned et al., 2008). Geoneutrino detection at two sites in the Pacific

ocean offers a possibility to constrain mantle uranium and thorium abundances, and to examine the thermochemical piles hypothesis. In general, adding an observation datum with a reasonably low uncertainty ($\lesssim 15\%$) to Figure 5 would substantially tighten the constraints on mantle radioactivity abundance and distribution. Contingent on enthusiastic involvement of the geophysical community, experimental neutrino research can contribute significantly to our understanding of Earth’s interior.

Acknowledgments

We gratefully acknowledge support for this research from NSF EAR 0855791 CSEDI Collaborative Research: Neutrino Geophysics: Collaboration Between Geology & Particle Physics, and Hawaii Pacific University’s Trustees’ Scholarly Endeavors Program.

References

- Allègre, C. J., Poirier, J.-P., Humler, E., Hofmann, A. W., 1995. The chemical composition of the Earth. *Earth Planet. Sci. Lett.* 134 (3–4), 515–526. doi:10.1016/0012-821X(95)00123-T.
- Araki, T., et al., 2005. Experimental investigation of geologically produced antineutrinos with KamLAND. *Nature* 436 (7050), 499–503. doi:10.1038/nature03980.
- Arevalo, Jr, R., McDonough, W. F., 2010. Chemical variations and regional diversity observed in MORB. *Chem. Geol.* 271 (1-2), 70–85. doi:10.1016/j.chemgeo.2009.12.013.

- Arevalo, Jr., R., McDonough, W. F., Luong, M., 2009. The K/U ratio of the silicate Earth: Insights into mantle composition, structure and thermal evolution. *Earth Planet. Sci. Lett.* 278 (3-4), 361–369. doi:10.1016/j.epsl.2008.12.023.
- Bassin, C., Laske, G., Masters, G., 2000. The current limits of resolution for surface wave tomography in North America. *Eos Trans. AGU* 81 (48), F897. Data available at <http://igppweb.ucsd.edu/~gabi/crust2.html>.
- Bellini, G., et al., 2010. Observation of geo-neutrinos. *Phys. Lett. B* 687 (4-5), 299–304. doi:10.1016/j.physletb.2010.03.051.
- Boyet, M., Carlson, R. W., 2006. A new geochemical model for the Earth’s mantle inferred from ^{146}Sm — ^{142}Nd systematics. *Earth Planet. Sci. Lett.* 250 (1-2), 254–268. doi:10.1016/j.epsl.2006.07.046.
- Campbell, I. H., O’Neill, H., 2012. Evidence against a chondritic Earth. *Nature* 483 (7391), 553–558. doi:10.1038/nature10901.
- Davies, J. H., Davies, D. R., 2010. Earth’s surface heat flux. *Solid Earth* 1 (1), 5–24. doi:10.5194/se-1-5-2010.
- Dye, S. T., 2010. Geo-neutrinos and silicate earth enrichment of U and Th. *Earth Planet. Sci. Lett.* 297 (1-2), 1–9. doi:10.1016/j.epsl.2010.06.012.
- Dye, S. T., 2012. Geo-neutrinos as indicators of the origin and thermal history of the Earth. arXiv:1111.6099v2.
- Dziewonski, A. M., Anderson, D. L., 1981. Preliminary reference Earth

- model. *Phys. Earth Planet. Int.* 25 (4), 297–356. doi:10.1016/0031-9201(81)90046-7.
- Enomoto, S., Ohtani, E., Inoue, K., Suzuki, A., 2007. Neutrino geophysics with KamLAND and future prospects. *Earth Planet. Sci. Lett.* 258 (1-2), 147–159. doi:10.1016/j.epsl.2007.03.038.
- Fiorentini, G., Fogli, G. L., Lisi, E., Mantovani, F., Rotunno, A. M., 2012. Mantle geoneutrinos in KamLAND and Borexino. arXiv:1204.1923v1.
- Fiorentini, G., Lissia, M., Mantovani, F., 2007. Geo-neutrinos and earth’s interior. *Phys. Rep.* 453 (5-6), 117–172. doi:10.1016/j.physrep.2007.09.001.
- Fitoussi, C., Bourdon, B., 2012. Silicon isotope evidence against an enstatite chondrite Earth. *Science* 335 (6075), 1477–1480. doi:10.1126/science.1219509.
- Gando, A., et al., 2011. Partial radiogenic heat model for Earth revealed by geoneutrino measurements. *Nature Geosci.* 4 (9), 647–651. doi:10.1038/ngeo1205.
- Hart, S. R., Zindler, A., 1986. In search of a bulk-Earth composition. *Chem. Geol.* 57 (3–4), 247–267. doi:10.1016/0009-2541(86)90053-7.
- Hofmann, A. W., 1997. Mantle geochemistry: The message from oceanic volcanism. *Nature* 385 (6613), 219–229. doi:10.1038/385219a0.
- Jaupart, C., Labrosse, S., Mareschal, J.-C., 2007. Temperatures, heat and energy in the mantle of the Earth. In G. Schubert, editor in chief , D. Bercovici, eds., *Mantle Dynamics*, vol. 7 of *Treatise on Geophysics*,

- chap. 7.06, 253–303. Elsevier Scientific Publishing Company, New York. doi:10.1016/B978-044452748-6.00114-0.
- Javoy, M., et al., 2010. The chemical composition of the Earth: Enstatite chondrite models. *Earth Planet. Sci. Lett.* 293 (3-4), 259–268. doi:10.1016/j.epsl.2010.02.033.
- Krauss, L. M., Glashow, S. L., Schramm, D. N., 1984. Antineutrino astronomy and geophysics. *Nature* 310 (5974), 191–198. doi:10.1038/310191a0.
- Learned, J. G., Dye, S. T., Pakvasa, S., 2008. Hanohano: A deep ocean anti-neutrino detector for unique neutrino physics and geophysics studies. arXiv:0810.4975v1, Published in the Proceedings of the Twelfth International Workshop on Neutrino Telescopes, Venice, March 2007.
- Mantovani, F., Carmignani, L., Fiorentini, G., Lissia, M., 2004. Antineutrinos from Earth: A reference model and its uncertainties. *Phys. Rev. D* 69 (1), 013001. doi:10.1103/PhysRevD.69.013001.
- McDonough, W. F., 2003. Compositional model for the Earth’s core. In H. D. Holland, K. K. Turekian, eds., *The Mantle and Core*, vol. 2 of *Treatise on Geochemistry*, chap. 2.15, 547–568. Elsevier Scientific Publishing Company, Oxford. doi:10.1016/B0-08-043751-6/02015-6.
- McDonough, W. F., Sun, S., 1995. The composition of the Earth. *Chem. Geol.* 120 (3-4), 223–253. doi:10.1016/0009-2541(94)00140-4.
- Murakami, M., Ohishi, Y., Hirao, N., Hirose, K., 2012. A perovskitic lower mantle inferred from high-pressure, high-temperature sound velocity data. *Nature* 485 (7396), 90–94. doi:10.1038/nature11004.

- O'Neill, H. S., Palme, H., 2008. Collisional erosion and the non-chondritic composition of the terrestrial planets. *Philosophical Transactions of the Royal Society A: Mathematical, Physical and Engineering Sciences* 366 (1883), 4205–4238. doi:10.1098/rsta.2008.0111.
- Palme, H., O'Neill, H. S. C., 2003. Cosmochemical estimates of mantle composition. In H. D. Holland, K. K. Turekian, eds., *The Mantle and Core*, vol. 2 of *Treatise on Geochemistry*, chap. 2.01, 1–38. Elsevier Scientific Publishing Company, Oxford. doi:10.1016/B0-08-043751-6/02177-0.
- Plank, T., Langmuir, C. H., 1998. The chemical composition of subducting sediment and its consequences for the crust and mantle. *Chem. Geol.* 145 (3-4), 325–394. doi:10.1016/S0009-2541(97)00150-2.
- Ritsema, J., van Heijst, H. J., Woodhouse, J. H., 1999. Complex shear wave velocity structure imaged beneath Africa and Iceland. *Science* 286 (5446), 1925–1928. doi:10.1126/science.286.5446.1925.
- Rudnick, R. L., Gao, S., 2003. Composition of the continental crust. In H. D. Holland, K. K. Turekian, eds., *The Crust*, vol. 3 of *Treatise on Geochemistry*, chap. 3.01, 1–64. Elsevier Scientific Publishing Company, Oxford. doi:10.1016/B0-08-043751-6/03016-4.
- Salters, V. J. M., Stracke, A., 2004. Composition of the depleted mantle. *Geochem. Geophys. Geosyst.* 5 (5), Q05B07. doi:10.1029/2003GC000597.
- Su, W.-j., Dziewonski, A. M., 1997. Simultaneous inversion for 3-D variations in shear and bulk velocity in the mantle. *Phys. Earth Planet. Int.* 100 (1-4), 135–156. doi:10.1016/S0031-9201(96)03236-0.

- Turcotte, D. L., Schubert, G., 2002. *Geodynamics, Applications of Continuum Physics to Geological Problems*. Cambridge University Press, second edn.
- Wang, Y., Wen, L., 2004. Mapping the geometry and geographic distribution of a very low velocity province at the base of the Earth's mantle. *J. Geophys. Res.* 109 (B10), B10305. doi:10.1029/2003JB002674.
- Warren, P. H., 2011. Stable-isotopic anomalies and the accretionary assemblage of the Earth and Mars: A subordinate role for carbonaceous chondrites. *Earth Planet. Sci. Lett.* 311 (1–2), 93–100. doi:10.1016/j.epsl.2011.08.047.
- Wen, L., Silver, P., James, D., Kuehnel, R., 2001. Seismic evidence for a thermo-chemical boundary at the base of the Earth's mantle. *Earth Planet. Sci. Lett.* 189 (3–4), 141–153. doi:10.1016/S0012-821X(01)00365-X.
- White, W. M., Klein, E. M., 2013, projected. The oceanic crust. In H. D. Holland, K. K. Turekian, eds., *The Crust, Treatise on Geochemistry*, chap. 14. Elsevier Scientific Publishing Company, Oxford, second edn.
- Workman, R. K., Hart, S. R., 2005. Major and trace element composition of the depleted MORB mantle (DMM). *Earth Planet. Sci. Lett.* 231 (1-2), 53–72. doi:10.1016/j.epsl.2004.12.005.
- Wurm, M., et al., 2012. The next-generation liquid-scintillator neutrino observatory LENA. *Astroparticle Phys.* 35 (11), 685–732. doi:10.1016/j.astropartphys.2012.02.011.

Zhang, J., Dauphas, N., Davis, A. M., Leya, I., Fedkin, A., 2012. The proto-Earth as a significant source of lunar material. *Nature Geosci.* 5 (4), 251–255. doi:10.1038/ngeo1429.

Table 1: Relevant atomic parameters. Atomic mass M in unified atomic mass units ($1u = 1.661 \times 10^{-27}$ kg), half-life $\tau_{1/2}$ in Gyr, decay constant $\lambda = \ln(2)/\tau_{1/2}$ in 10^{-18} s^{-1} , energy available for radiogenic heating Q_h in pJ per decay. [†]Non-integer $\bar{\nu}_e$'s per chain value for ^{40}K reflects branching into β decay and electron capture.

	^{238}U	^{235}U	^{232}Th	^{40}K	Reference
Isotopic ratio X	0.9927	0.007204	1.0000	117 ppm	www.nist.gov
Atomic mass M	238.051	235.044	232.038	39.9640	www.nist.gov
Half life $\tau_{1/2}$	4.468	0.704	14.05	1.265	www.nucleide.org
Decay constant λ	4.916	31.2	1.563	17.36	
Energy to heat Q_h	7.648	7.108	6.475	0.110	Dye (2012)
$\bar{\nu}_e$'s per chain n	6	4	4	0.8928 [†]	

Table 2: Chemical composition estimates for HPEs, corresponding radiogenic power, and the mantle Urey ratio. Bulk silicate Earth (BSE): cosmochemical, geochemical, and geodynamical estimates (see text). Bulk continental crust (CC; includes sediments): R&G (Rudnick and Gao, 2003). Bulk oceanic crust (OC; includes sediments): W&K (White and Klein, 2013, projected), P&L (Plank and Langmuir, 1998). Bulk mantle (BM) calculated from eqn. 4. Depleted Mantle (DM), MORB-source: W&H (Workman and Hart, 2005), S&S (Salters and Stracke, 2004), A&McD (Arevalo and McDonough, 2010). *Assumes that entire mantle is DM.

	BSE			CC (incl. sed.)	OC (incl. sed.)	
	Cosmochem.	Geochem.	Geodyn.	R&G	W&K, P&L	
A_U in ppb	12 ± 2	20 ± 4	35 ± 4	1.47 ± 0.26 ppm	0.15 ± 0.02 ppm	
A_{Th} in ppb	43 ± 4	80 ± 13	140 ± 14	6.33 ± 0.50 ppm	0.53 ± 0.04 ppm	
A_K in ppm	129 ± 26	280 ± 60	350 ± 35	1.63 ± 0.12 wt%	0.17 ± 0.01 wt%	
Th/U	3.6	4.0	4.0	4.3	3.6	
K/U	10900	14000	10000	11100	11400	
Power in TW	11 ± 2	20 ± 4	33 ± 3	7.8 ± 0.9	0.21 ± 0.02	

	BM			DM		
	Cosmochem.	Geochem.	Geodyn.	W&H	S&S	A&McD
A_U in ppb	3.8 ± 2.8	12 ± 4	27 ± 4	3.2 ± 0.5	4.7 ± 1.4	8 ± 2
A_{Th} in ppb	8.2 ± 5.0	46 ± 12	106 ± 14	7.9 ± 1.1	13.7 ± 4.1	22 ± 4
A_K in ppm	40 ± 27	192 ± 61	263 ± 36	50 ± 8	60 ± 17	152 ± 30
Th/U	2.1	3.8	3.9	2.5	2.9	2.8
K/U	10600	16000	9700	15600	12800	19000
Power in TW	2.9 ± 2.0	12 ± 4	25 ± 3	$2.8 \pm 0.4^*$	$4.1 \pm 1.2^*$	$7.5 \pm 1.5^*$
Mantle Urey ratio	0.07 ± 0.05	0.3 ± 0.1	0.7 ± 0.1			

Table 3: (a) Earth reservoir masses. Values from PREM (Dziewonski and Anderson, 1981) and CRUST2.0 (Bassin et al., 2000).

Reservoir		Mass in kg	Reference
Earth	m_E	5.9732×10^{24}	PREM
Continental crust (incl. sed.)	m_{CC}	2.14×10^{22}	CRUST2.0
Oceanic crust (incl. sed.)	m_{OC}	0.63×10^{22}	CRUST2.0
Crust (=cont.+oc.)	m_C	2.77×10^{22}	
Mantle	m_M	4.0024×10^{24}	PREM
BSE (=mantle+crust)	m_{BSE}	4.0303×10^{24}	

Table 4: Enrichment factors (calculated from eqn. 6) and geoneutrino fluxes for various models of HPE abundances and distribution. Results for spherically symmetric models (UNIF, EL) are reported including 1σ uncertainties. For models with lateral variation in HPE abundances (P1, P2, TOMO), the surface average, minimum and maximum values ($min\ ave^{max}$) based on central value of compositional estimates are shown.

BSE	DM	Enrichment E			Model	Geoneutrino flux Φ in $\text{cm}^{-2} \mu\text{s}^{-1}$			
		U	Th	K		^{238}U	^{235}U	^{232}Th	^{40}K
Spherically symmetric models — EM is 10% of mantle by mass									
cosnochem.	—	—	—	—	UNIF	0.19 ± 0.14	0.0059 ± 0.0043	0.090 ± 0.055	0.75 ± 0.49
geochem.	—	—	—	—	UNIF	0.60 ± 0.21	0.019 ± 0.007	0.50 ± 0.14	3.5 ± 1.1
geodyn.	—	—	—	—	UNIF	1.4 ± 0.2	0.042 ± 0.006	1.2 ± 0.2	4.8 ± 0.7
cosnochem.	A&McD	< 1	< 1	< 1	EL	—	—	—	—
cosnochem.	S&S	1–5.5	1–1.1	1–2.6	EL	$0.23\text{--}0.31$	$0.0073\text{--}0.0098$	0.15	1.1–1.2
cosnochem.	W&H	2.9 ± 8.8	1.4 ± 6.6	1–4.6	EL	$0.18^{+0.11}_{-0.02}$	$0.0057^{+0.0033}_{-0.0007}$	$0.089^{+0.043}_{-0.003}$	0.9–1.2
geochem.	A&McD	6.0 ± 6.1	12 ± 7	3.6 ± 4.7	EL	$0.55^{+0.19}_{-0.15}$	$0.017^{+0.006}_{-0.005}$	0.44 ± 0.13	$3.4^{+1.0}_{-0.6}$
geochem.	S&S	17 ± 12	24 ± 14	23 ± 14	EL	0.51 ± 0.21	0.016 ± 0.007	0.42 ± 0.15	3.0 ± 1.2
geochem.	W&H	29 ± 15	49 ± 18	29 ± 13	EL	0.50 ± 0.18	0.015 ± 0.005	0.40 ± 0.12	2.9 ± 0.9
geodyn.	A&McD	25 ± 8	39 ± 12	8.3 ± 4.2	EL	1.1 ± 0.3	0.035 ± 0.008	0.94 ± 0.21	4.4 ± 0.9
geodyn.	S&S	49 ± 19	69 ± 26	35 ± 14	EL	1.1 ± 0.3	0.034 ± 0.011	0.92 ± 0.29	3.9 ± 1.2
geodyn.	W&H	76 ± 18	126 ± 26	44 ± 11	EL	1.1 ± 0.2	0.033 ± 0.007	0.91 ± 0.17	3.9 ± 0.7
Laterally variable cartoon models — EM is 10% of mantle by mass									
geochem.	A&McD	6.0	12	3.6	P1	$0.46\ 0.56^{0.69}$	$0.014\ 0.017^{0.022}$	$0.32\ 0.45^{0.62}$	$3.0\ 3.4^{3.9}$
geochem.	A&McD	6.0	12	3.6	P2	$0.51\ 0.56^{0.64}$	$0.016\ 0.017^{0.020}$	$0.39\ 0.45^{0.55}$	$3.2\ 3.4^{3.7}$
Seismic tomography-based models — EM is 9.5% of mantle by mass									
cosnochem.	A&McD	< 1	< 1	< 1		—	—	—	—
cosnochem.	S&S	< 1	< 1	< 1		—	—	—	—
cosnochem.	W&H	3.0	1.4	< 1	TOMO	$0.17\ 0.18^{0.20}$	$0.0055\ 0.0057^{0.0063}$	$0.088\ 0.089^{0.091}$	—
geochem.	A&McD	6.3	12	3.8	TOMO	$0.50\ 0.56^{0.67}$	$0.016\ 0.017^{0.021}$	$0.38\ 0.45^{0.60}$	$3.2\ 3.4^{3.8}$
geochem.	S&S	17	26	24	TOMO	$0.42\ 0.53^{0.73}$	$0.013\ 0.016^{0.023}$	$0.33\ 0.43^{0.63}$	$2.4\ 3.1^{4.4}$
geochem.	W&H	30	51	31	TOMO	$0.39\ 0.52^{0.76}$	$0.012\ 0.016^{0.024}$	$0.30\ 0.42^{0.65}$	$2.3\ 3.0^{4.5}$
geodyn.	A&McD	26	41	8.6	TOMO	$0.9\ 1.2^{1.7}$	$0.028\ 0.036^{0.053}$	$0.72\ 0.98^{1.49}$	$3.9\ 4.4^{5.6}$
geodyn.	S&S	51	72	36	TOMO	$0.8\ 1.1^{1.8}$	$0.025\ 0.035^{0.055}$	$0.67\ 0.97^{1.5}$	$3.0\ 4.1^{6.2}$
geodyn.	W&H	80	132	46	TOMO	$0.8\ 1.1^{1.8}$	$0.024\ 0.035^{0.055}$	$0.64\ 0.95^{1.55}$	$3.0\ 4.1^{6.2}$

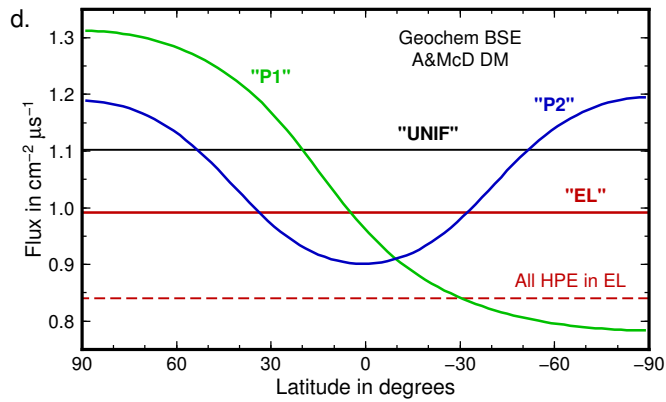
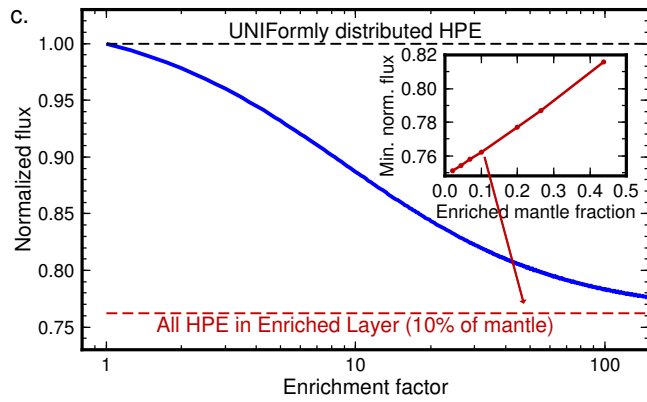
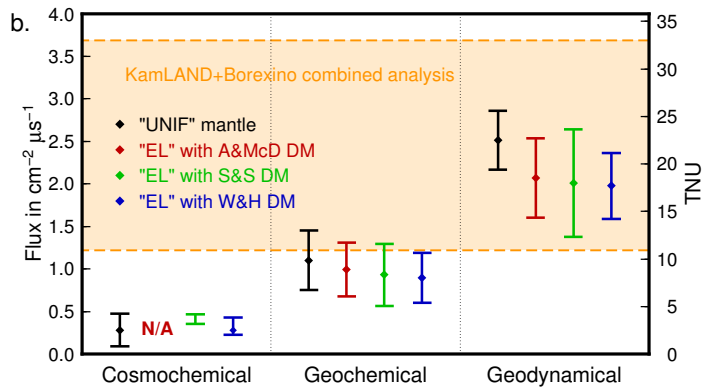
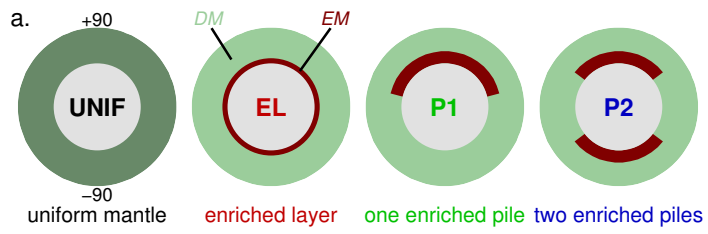
Table 5: Mass fraction and enrichment factors for the enriched mantle reservoir obtained for various δV_s cut-off contours in the TOMO model.

δV_s cut-off	EM mass. frac.	enrichment factor		
	F^{EM}	E_U	E_{Th}	E_K
−0.25 %	9.5 %	6.3	13	3.8
−0.50 %	4.4 %	13	26	7.0
−0.75 %	1.8 %	30	63	16
−1.00 %	0.71 %	72	155	38

Table 6: Input parameters for calculation of detection error of mantle geoneutrino flux (eqn.12). Values in TNU unless stated otherwise.

Quantity	Site 1		Site 2		Reference
	Value	Error	Value	Error	
R_M cosmochem.	3.0	–	2.7	–	this study
R_M geochem.	11	–	8.2	–	this study
R_M geodyn.	27	–	17	–	this study
R_C	2.6	13 %	3.6	13 %	this study
R_r	0.9	5 %	0.6	5 %	Dye (2012)
R_{bg}	2.3	0.3	2.3	0.3	Bellini et al. (2010)
ε	–	2 %	–	2 %	Dye (2010)

Figure 1: (a) Cartoon model gallery. Bulk mantle in dark green, depleted mantle (DM) in light green, and enriched mantle (EM) in dark red. Models UNIF and EL are spherically symmetric, models P1 and P2 are axially symmetric. (b) Calculated geoneutrino fluxes from $^{238}\text{U}+^{232}\text{Th}$ decay in a spherically symmetric mantle (black, red, green, and blue data points and error bars) compared to experimental observation (yellow region, combined analysis of KamLAND and Borexino data; Fiorentini et al., 2012). Conversion between $\text{cm}^{-2}\mu\text{s}^{-1}$ and TNU on right-hand vertical axis assumes $\text{Th}/\text{U}=3.9$. (c) Effect of HPE sequestration in a deep mantle layer on the geoneutrino flux at the surface. Main plot shows flux reduction with increasing enrichment of the deep-seated reservoir. Dependence of the maximum flux reduction on the enriched reservoir size is shown in the inset. (d) Geoneutrino flux variation along latitude for cartoon models shown in panel ‘a’ using geochemical BSE and A&McD DM compositional estimates.



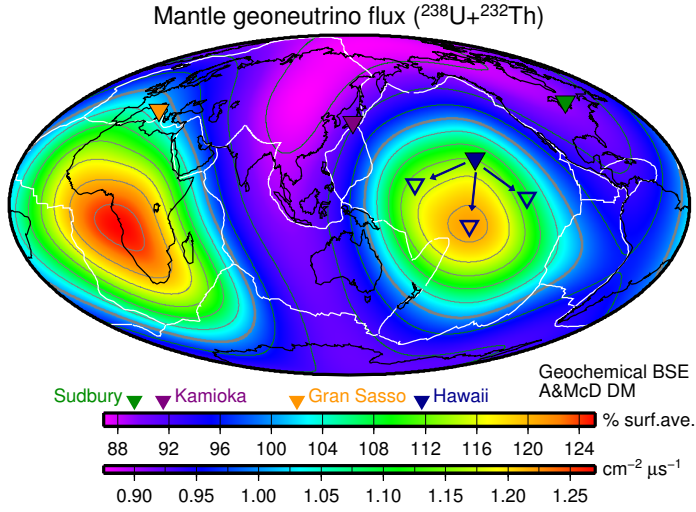


Figure 2: Global map of geoneutrino flux from $^{238}\text{U}+^{232}\text{Th}$ decay in the mantle calculated for the TOMO model using geochemical BSE and A&McD DM compositional estimates. A uniform radius for the crust–mantle boundary is used (6346.6 km), flux is evaluated at radius of 6371 km and shown as percentage of the surface-averaged value (color scale) with contour lines at 4% intervals. Continental outlines (black), plate boundaries (white), and locations of geoneutrino detectors are plotted: Kamioka, Japan (KamLAND, operational); Gran Sasso, Italy (Borexino, operational); Sudbury, Canada (SNO+, online 2013); Hawaii (Hanohano, proposed; transportable detector as illustrated by open triangles and arrows).

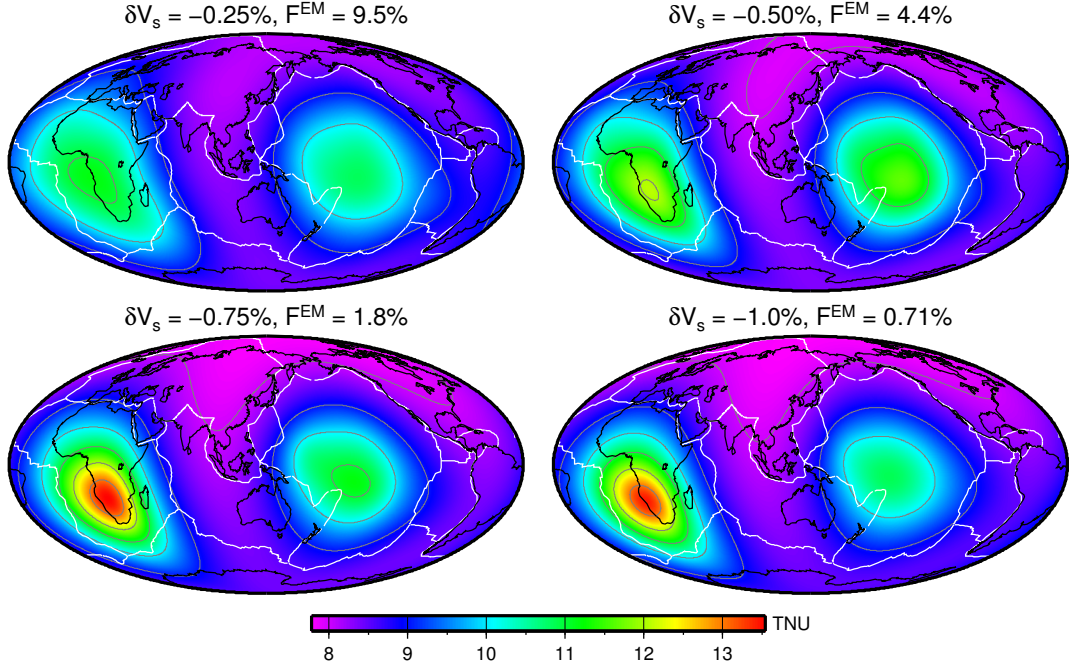
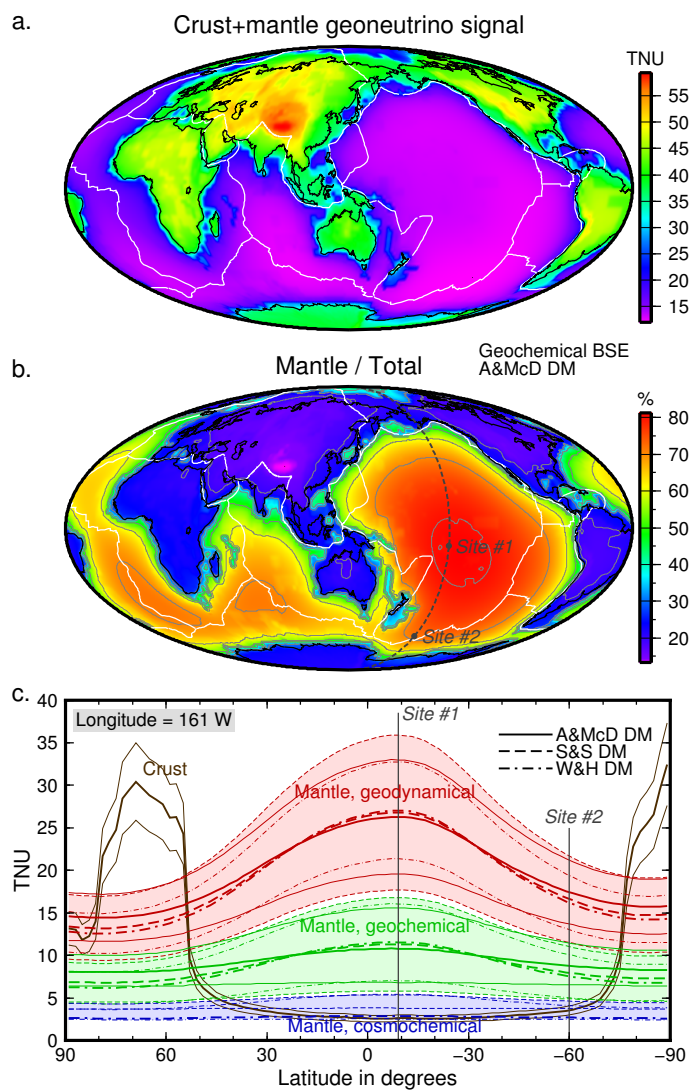


Figure 3: Global map of geoneutrino flux from $^{238}\text{U} + ^{232}\text{Th}$ decay in the mantle calculated for the TOMO model using geochemical BSE and A&McD DM compositional estimates, and several different cut-off δV_s contours (indicated above each map together with the resulting mass fraction of the enriched mantle reservoir F^{EM}). A unique radius for the crust–mantle boundary is used (6346.6 km), flux is evaluated at radius of 6371 km and shown in TNU with contour lines at 1 TNU intervals. Continental outlines (black) and plate boundaries (white) are plotted. Color scale is identical for all four maps.

Figure 4: (a) Global map of predicted total geoneutrino signal ($^{238}\text{U}+^{232}\text{Th}$, crust+mantle) in TNU. Mantle anti-neutrino emission model same as in Fig. 2. Crustal prediction based on CRUST2.0 structure, and R&G, W&K and P&L compositional estimates (see text). Topography of the crust–mantle boundary is accounted for, geoneutrino fluxes are evaluated at zero elevation in oceanic areas and at Earth’s surface in continental regions. Continental outlines (black) and plate boundaries (white) are shown. (b) Map showing the fraction of total signal from panel ‘a’ that is contributed by the mantle; the remainder is the crustal contribution. Contour lines at 10% intervals. (c) Variation of predicted geoneutrino signal along 161°W meridian which intersects the Pacific mantle flux maximum at 9°S . Crustal prediction shown in brown. Mantle predictions based on cosmochemical, geochemical, and geodynamical BSE estimates shown in blue, green, and red, respectively. Central values (thick curves) and 1σ uncertainty limits (thin lines and shading) are shown. Two oceanic measurement sites are proposed (shown in panels ‘b’ and ‘c’) in order to constrain Earth’s mantle architecture.



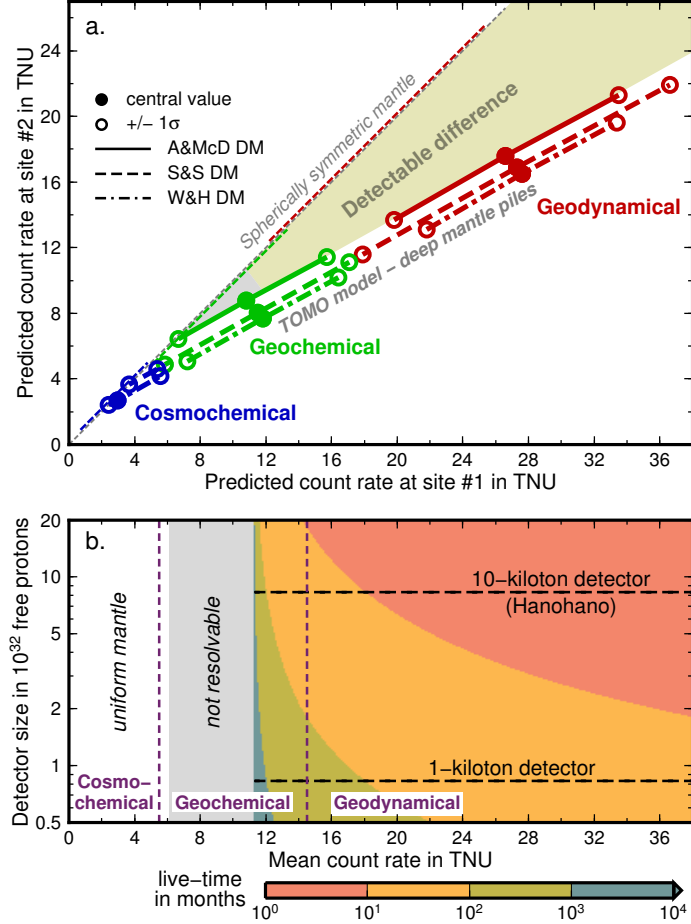


Figure 5: (a) Mantle geoneutrino count rate in TNU at sites #1 (horizontal axis) and #2 (vertical axis) as predicted from cosmochemical (blue), geochemical (green) and geodynamical (red) BSE estimates, including 1σ uncertainties, using various DM estimates. Predictions for a spherically symmetric mantle, both homogeneous and layered, follow a straight line with slope 1. Predictions of TOMO model align along a gentler slope. The region of detectable difference between these two predictions is indicated. (b) The required detector exposure required to discriminate between the two predictions shown in terms of detector size (vertical axis) and live-time (color) as a function of mean count rate at sites #1 and #2 (horizontal axis).

Supplementary Figures

Figure S1: Global map of geoneutrino flux from $^{238}\text{U}+^{232}\text{Th}$ decay in the mantle calculated for the TOMO model for all combinations of BSE and DM compositional estimates. A unique radius for the crust–mantle boundary is used (6346.6 km), flux is evaluated at radius of 6371 km and shown in TNU. Continental outlines (black) and plate boundaries (white) are plotted. Middle column calculated using central values of the enrichment factor, right and left columns calculated at $\pm 1\sigma$ limits for the enrichment factor in each case. The color scale is common within each BSE estimate used. Empty maps labeled “N/A” reflect inconsistency for the particular combination of BSE and DM compositional estimates (enrichment factor smaller than one or even negative).

Figure S2: Same as Figure S1 except for the color scale, which is identical for all maps.

